INTERNATIONAL JOURNAL FOR NUMERICAL METHODS IN FLUIDS, VOL. 13, 1153–1170 (1991)

NUMERICAL SIMULATION OF THE REFLECTION OF A PLANAR SHOCK WAVE OVER A DOUBLE WEDGE

K. ITOH

National Aerospace Laboratory, Kakuda Research Center, Kakuda, Japan

K. TAKAYAMA

Shock Wave Research Center, Institute of Fluid Science, Tohoku University, Sendai, Japan

AND

G. BEN-DOR

Department of Mechanical Engineering, Pearlstone Center for Aeronautical Engineering Studies, Ben-Gurion University of the Negev, Beer Sheva, Israel

SUMMARY

A numerical code based on the upwind TVD scheme for simulating the various reflection processes of a planar shock wave over a concave or convex double wedge has been developed. The numerical results were compared with actual experiments and excellent agreement was obtained. The excellent agreement serves also as a validation of the shock-capturing performance of the numerical scheme

KEY WORDS Shock wave Reflections Holographic interfermetry

INTRODUCTION

When a planar shock wave collides with an oblique straight surface, it reflects over the surface either as a Mach reflection (MR) or as a regular reflection (RR) depending upon the incident shock wave Mach number M_i and the reflecting wedge angle θ_w.

Schematic illustrations of the wave configurations of a regular reflection and a Mach reflection are shown in Figures 1(a) and 1(b) respectively. The regular reflection wave configuration consists of two discontinuities, namely the incident shock wave, i, and the reflected shock wave, r, which meet on the reflecting wedge surface at the reflection point, R. The Mach reflection wave configuration consists of four discontinuities, i.e. three shock waves, namely the incident shock wave, i, the reflected shock wave, r, and the Mach stem, m, and one slipstream, s. These four discontinuities meet at a single point, the triple point, T, which is located above the reflecting surface and moves away from it along a straight line (chain line in Figure 1(b)).

For any incident shock wave Mach number M_i, there is a critical wedge angle, known as the transition wedge angle, $\theta_w^{tr}|_{M_i}$ at which the RR⇔MR transition occurs. The regular reflection takes place for $\theta_w > \theta_w^{tr}|_{M_i}$ and the Mach reflection for $\theta_w < \theta_w^{tr}|_{M_i}$.

In the case of the reflection of a planar shock wave over a single wedge, such as that in Figure 1, the RR⇔MR transition does not actually take place. Depending upon the initial values of M_i and

0271–2091/91/191153–18$09.00

Received June 1990
Revised February 1991

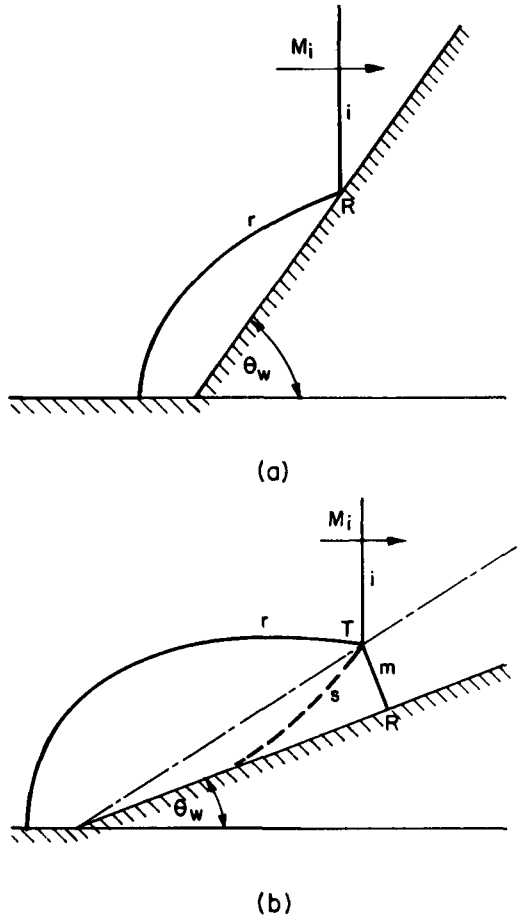

Figure 1. Schematic illustrations of the wave configurations of (a) regular reflection, RR, and (b) Mach reflection, MR

θ_w, either a regular reflection or a Mach reflection is formed. Since both M_i and θ_w remain constant, the originally formed type of reflection does not transit to the other type.

This is not the case when a planar shock wave collides with a wedge which has a change in slope of the surface from θ_w^1 to θ_w^2. In general, two different double wedges are possible depending upon whether θ_w^1 is greater or smaller than θ_w^2. If $\Delta\theta_w$ is the inclination of the second surface with respect to the first one, i.e. $\Delta\theta_w = \theta_w^2 - \theta_w^1$, then the double wedge is concave when $\Delta\theta_w > 0$ and convex when $\Delta\theta_w < 0$. Schematic drawings of a concave and convex double wedge are shown in Figures 2(a) and 2(b) respectively.

The reflection of a planar shock wave over a double wedge is a relatively new topic of research. The first experiments regarding this topic were conducted by Takayama *et al.*[1] A comprehensive study was later made by Ben-Dor *et al.*[2] In their study they established that for a given incident shock wave Mach number M_i, there are seven different domains of reflection processes in the (θ_w^1, θ_w^2)-plane.

The domains of the different types of reflection processes of a planar shock wave over a double wedge in the (θ_w^1, θ_w^2)-plane are shown in Figure 3. The line $\Delta\theta_w = 0$ divides the (θ_w^1, θ_w^2)-plane into the domains of a concave double wedge, $\Delta\theta_w > 0$ (Figure 2(a)), and a convex double wedge,

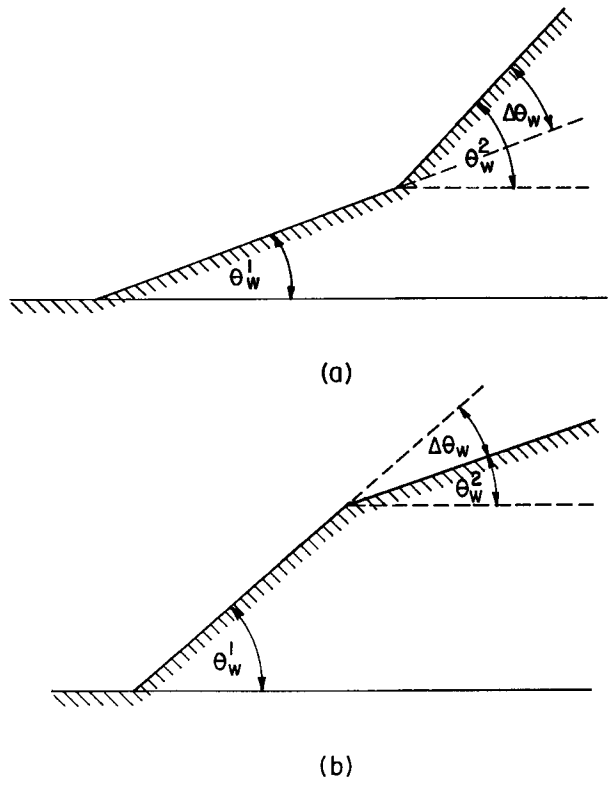

Figure 2. Schematic illustrations of (a) concave double wedge and (b) convex double wedge

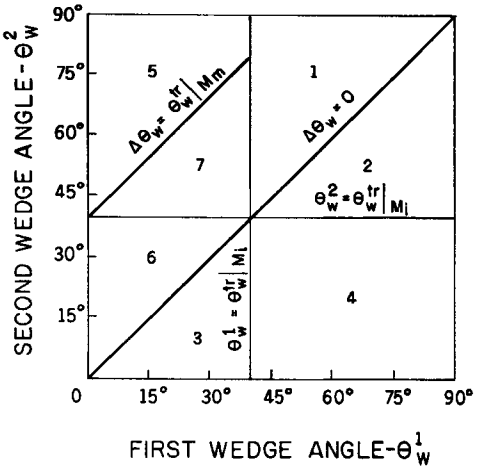

Figure 3. Domains of different types of reflection processes of a planar shock wave having a Mach number $M_i = 1{\cdot}3$ over a concave or convex double wedge. A summary of the reflection processes is given in Table I. θ_w^1, first wedge angle; θ_w^2, second wedge angle; $\Delta\theta_w = \theta_w^2 - \theta_w^1$; $\theta_w^{tr}|_{M_i}$, RR⇔MR transition wedge angle corresponding to incident shock wave Mach number M_i; $\theta_w^{tr}|_{M_m}$, RR⇔MR transition wedge angle corresponding to Mach stem Mach number M_m

$\Delta\theta_w<0$ (Figure 2(b)). The line $\theta_w^1=\theta_w^{tr}|_{M_i}$ (where $\theta_w^{tr}|_{M_i}$ is the RR⇔MR transition wedge angle corresponding to the incident shock wave Mach number M_i) determines the initial type of reflection over the first wedge surface. If $\theta_w^1<\theta_w^{tr}|_{M_i}$, then the incident shock wave reflects over the first wedge as a Mach reflection, MR (see Figure 1(b)). However, if $\theta_w^1>\theta_w^{tr}|_{M_i}$, then the reflection of the incident shock wave over the first wedge is a regular reflection, RR (see Figure 1(a)). The line $\theta_w^2=\theta_w^{tr}|_{M_i}$ determines the type of reflection which is finally obtained over the second wedge. The final reflection is an MR if $\theta_w^2<\theta_w^{tr}|_{M_i}$, while it is an RR when $\theta_w^2>\theta_w^{tr}|_{M_i}$. If the double wedge surface is concave, i.e. $\Delta\theta_w>0$ (see Figure 2(a)) and if the initial reflection over the first surface is an MR (i.e. $\theta_w^1<\theta_w^{tr}|_{M_i}$), then the Mach stem of this MR reflects over the second surface either as an MR if $\Delta\theta_w<\theta_w^{tr}|_{M_m}$ or as an RR if $\Delta\theta_w>\theta_w^{tr}|_{M_m}$. Here $\theta_w^{tr}|_{M_m}$ is the RR⇔MR transition wedge angle corresponding to the Mach stem Mach number M_m. It is important to note that M_m is always greater than M_i. However, for a large range of incident shock wave numbers the RR⇔MR transition wedge angle depends very slightly on the incident shock wave Mach number. Therefore for most Mach numbers it is quite practical to assume that $\theta_w^{tr}|_{M_i}=\theta_w^{tr}|_{M_m}$. The foregoing discussion regarding the various types of reflection processes of a planar shock wave over a concave or convex double wedge is summarized in Table I.

The above-mentioned study of Ben-Dor *et al.*[2] was aimed at establishing the domains and boundaries of the various types of reflection processes of a planar shock wave over a concave or convex double wedge in the (θ_w^1, θ_w^2)-plane. The need to understand this phenomenon is quite obvious if one considers the strong wave interaction in the flow field of SCRAM jet engine inlets, where the wave structures have many similarities to those resulting from wave interaction with a double wedge. There is little doubt that the RR→MR transition in the inlets is the key to the start–unstart problem of the inlets. Furthermore, the vortex sheet generated by the shock wave interactions may cause non-linear increments of the heat flux on the blunt noses of the cowl and strut of the inlets. It may be also useful to better understand ground-explosion-generated blast wave interactions with man-made structures which have shapes similar to that of a double wedge.[3]

The aim of the present study is to develop a numerical method which can capture the above-mentioned reflection processes with high resolution and to obtain a reliability test of the numerical method by comparing its results with actual shock tube experiments visualized using double-exposure holographic interferometry. The present numerical method is based on the upwind TVD scheme, which has an excellent shock-capturing performance. It was applied to simulate the shock reflection processes over various combinations of double wedges. Generally, however, the shock-capturing performance of TVD schemes is not guaranteed mathematically

Table I. Summary of the seven different reflection processes which can occur over a concave or convex double wedge

	θ_w^1	θ_w^2	$\Delta\theta_w$	Reflection over first surface	Reflection over second surface	Domain in Figure 1
Concave	$>\theta_w^{tr}$	$>\theta_w^{tr}$	—	RR	RR	1
double	$<\theta_w^{tr}$	$>\theta_w^{tr}$	$>\theta_w^{tr}$	MR	RR → RR	5
wedge	$<\theta_w^{tr}$	$>\theta_w^{tr}$	$<\theta_w^{tr}$	MR	MR → RR	7
	$<\theta_w^{tr}$	$<\theta_w^{tr}$	$<\theta_w^{tr}$	MR	MR → MR	6
Convex	$>\theta_w^{tr}$	$>\theta_w^{tr}$	—	RR	RR	2
double	$>\theta_w^{tr}$	$<\theta_w^{tr}$	—	RR	MR	4
wedge	$<\theta_w^{tr}$	$<\theta_w^{tr}$	—	MR	MR	3

when the shock waves are oblique to the computational grid system. The most important aim of the present study is to validate the shock-capturing performance of this scheme when complicated shock interactions occur. The validations are obtained by comparing details of the numerical and experimental shock reflection processes.

NUMERICAL METHOD

The present numerical method is based on the TVD shock-capturing scheme originally developed by Harten[4] and later modified and applied by Itoh[5] and Yee[6] to the following Euler equations expressed in general curvilinear co-ordinates:

$$U_t + F_\xi + G_\eta = 0, \tag{1}$$

$$U = \hat{U}/J, \tag{2a}$$

$$F = (\xi_x \hat{F} + \xi_y \hat{G})/J, \tag{2b}$$

$$G = (\eta_x \hat{F} + \eta_y \hat{G})/J, \tag{2c}$$

$$J = \xi_x \eta_y - \xi_y \eta_x, \tag{2d}$$

$$\hat{U} = (\rho, \rho u, \rho v, e), \tag{2e}$$

$$\hat{F} = [\rho u, \rho u^2 + p, \rho uv, u(e+p)], \tag{2f}$$

$$\hat{G} = [\rho v, \rho uv, \rho v^2 + p, v(e+p)], \tag{2g}$$

where ρ, u, v, p and e denote density, velocities in the x- and y-directions, pressure and total energy per unit volume respectively. If the gas is assumed to behave as a perfect gas, its total energy per unit volume can be expressed as

$$e = p/(\gamma - 1) + \rho(u^2 + v^2)/2, \tag{3}$$

where γ is the ratio of specific heat capacities, i.e. C_p/C_v.

In the present study the Harten–Yee upwind TVD scheme was extended to the gas dynamic system (Equation (1)) using Roe's approximate Riemann solver.[7] Roe's approximate Riemann solver is an exact Riemann solver to the linearized system

$$U_t + \bar{A} U_x = 0, \qquad \bar{A} = \partial F/\partial U, \tag{4}$$

where $\bar{A}$ is the piecewise constant matrix which satisfies the jump conditions between two adjacent states:

$$F(U_R) - F(U_L) = A(\bar{U})(U_R - U_L). \tag{5}$$

This approximate Riemann solver gives the exact solution when the wave generated at the cell boundary is a single shock wave.

Using the operator-splitting technique, the resulting scheme is expressed as

$$U_{j,k}^{n+2} = L_\xi L_\eta L_\eta L_\xi U_{j,k}^n, \qquad U_{j,k}^n = U(n\Delta t, j\Delta\xi, k\Delta\eta), \tag{6}$$

where L_ξ and L_η are the TVD finite difference operators:

$$U_{j,k}^{n+1} = L_\xi U_{j,k}^n = U_{j,k}^n - \lambda(\tilde{F}_{j+1/2} - \tilde{F}_{j-1/2}), \qquad \lambda = \Delta t/\Delta\xi. \tag{7}$$

The numerical flux $\tilde{F}_{j+1/2}$ is evaluated at the cell boundary using the approximate Riemann solver:

$$\tilde{F}_{j+1/2} = F_{j+1,k} + F_{j,k} + R_{j+1/2}\Phi_{j+1/2}, \tag{8}$$

where $R_{j+1/2}$ is a matrix whose columns are the right eigenvectors of the flux Jacobian $A(U_{j+1/2})=(\partial F/\partial U)|_{j+1/2}$ which satisfies equation (5) as the average state of $U_{j+1,k}$ and $U_{j,k}$. $\Phi_{j+1/2}$ is a vector whose element $\phi^l_{j+1/2}$ consists of the numerical viscosity (identical to that of the first-order upwind scheme) and the second-order corrector limited to be TVD by the flux limiter. They are constructed for the signal conservation law in each characteristic field of the locally linearized system (equation (4)). The basic idea and the derivation of the TVD scheme used are briefly described in the following for the single conservation law, i.e.

$$v_t+f(v)_x=0. \tag{9}$$

Our requirement of the scheme is convergence to the weak solution of equation (9), which allows discontinuities to satisfy the jump condition which is derived so that the conservative property is maintained. The most important feature of the weak solution that the scheme should have is the monotonicity-preserving property. The scheme for equation (9) can be written in the conservative form

$$v_j^{n+1}=v_j^n-\lambda(f^n_{j+1/2}-f^n_{j-1/2}), \tag{10}$$

$$f_{j+1/2}=f(v_{j-k+1},\ldots,v_{j+k})=\tfrac{1}{2}[f(v_j)+f(v_{j+1})-Q_{j+1/2}\Delta_{j+1/2}v], \tag{11a}$$

$$Q_{j+1/2}=Q(v_{j-k+1},\ldots,v_{j+k}), \tag{11b}$$

$$\Delta_{j+1/2}=v_{j+1}-v_j, \tag{11c}$$

$$\lambda\equiv\Delta t/\Delta x. \tag{11d}$$

Now the scheme (equation (10)) is expressed in the parametric form

$$v_j^{n+1}=C^+_{j+1/2}v^n_{j+1}+(1-C^+_{j+1/2}-C^-_{j-1/2})v^n_j+C^-_{j-1/2}v^n_{j-1}, \tag{12}$$

$$C^{\pm}_{j+1/2}\equiv\tfrac{1}{2}\lambda(Q_{j+1/2}\mp a_{j+1/2}), \tag{13a}$$

$$a_{j+1/2}\equiv[f(v_{j+1})-f(v_j)]/(v_{j+1}-v_j). \tag{13b}$$

The basic idea of the TVD scheme derived by Harten[4] is to apply the following monotonicity-preserving property, which is the most important feature of the weak solution to the scheme:

$$\mathrm{TV}(v^{n+1})\leqslant\mathrm{TV}(v^n), \tag{14a}$$

$$\mathrm{TV}(v)\equiv\sum|v_{j+1}-v_j|. \tag{14b}$$

The following inequalities are the sufficient condition for the scheme to satisfy equation (14a) (this condition is known as the TVD conditon):

$$C^{\pm}_{j+1/2}\geqslant 0, \tag{15a}$$

$$1-C^+_{j+1/2}-C^-_{j-1/2}\geqslant 0. \tag{15b}$$

One of the best ways to construct the second-order scheme which satisfies the condition given by equations (15a) and (15b) is Harten's modified flux approach. Harten modified the flux in equation (9) with an additional flux g.

$$v_t+(f+g)_x=0, \tag{16}$$

and gave the first-order upwind scheme for equation (16):

$$v_j^{n+1}=v_j^n-\lambda(f_{j+1/2}-f_{j-1/2}), \tag{17}$$

$$f_{j+1/2}=\tfrac{1}{2}(f_j+f_{j+1}+g_j+g_{j+1}-|a_{j+1/2}+\beta_{j+1/2}|\Delta_{j+1/2}v), \tag{18a}$$

$$\beta_{j+1/2}=(g_{j+1}-g_j)/(v_{j+1}-v_j). \tag{18b}$$

Harten further constructed the additonal flux function g_j so that the scheme satisfies equations (15a) and (15b) and is second-order scheme for equation (9). The advantage of this approach is that the condition given by equation (15a) is automatically satisfied. Hence only the conditon given by equation (15b) need be considered, together with the following requirements for which the scheme is second-order for equation (9):

$$g_j=g_{j+1/2}+O(\Delta^2)=g_{j-1/2}+O(\Delta^2), \tag{19a}$$

$$g_{j+1/2}\equiv\sigma_{j+1/2}\Delta_{j+1/2}v, \tag{19b}$$

$$\sigma_{j+1/2}\equiv\tfrac{1}{2}(|a_{j+1/2}|-\lambda a_{j+1/2}^2). \tag{19c}$$

After some calculations one can readily obtain the range for the function g_j so that the scheme is the second-order TVD if $\operatorname{sgn}(g_{j+1/2})=\operatorname{sgn}(g_{j-1/2})$:

$$\min(|g_{j+1/2}|, |g_{j-1/2}|)\leqslant|g_j|\leqslant\max[\min(|g_{j+1/2}|, 2|g_{j-1/2}|),\ \min(2|g_{j+1/2}|, |g_{j-1/2}|)]. \tag{20}$$

For the case $\operatorname{sgn}(g_{j+1/2})\neq\operatorname{sgn}(g_{j-1/2})$ one cannot obtain a second-order TVD using this approach; therefore one should set $g_j=0$ and the scheme degenerates to a first-order scheme. Hence the constructed g_j, which is aimed at limiting the numerical flux to preserve the monotonicity property, is temed the flux limiter. Yee modified the above-described Harten TVD scheme by eliminating $\sigma_{j+1/2}$ from $g_{j+1/2}$ as follows:[6]

$$f_{j+1/2}=\tfrac{1}{2}[f_j+f_{j+1}+\sigma_{j+1/2}(g_j+g_{j+1})-|a_{j+1/2}+\beta_{j+1/2}|\Delta_{j+1/2}v], \tag{21}$$

$$\beta_{j+1/2}=\sigma_{j+1/2}(g_{j+1}-g_j)/(v_{j+1}-v_j), \tag{22a}$$

$$g_j=g(g_{j+1/2}, g_{j-1/2}), \tag{22b}$$

as well as equation (20),

$$g_{j+1/2}=\Delta_{j+1/2}v. \tag{22c}$$

The foregoing scheme, known as the Harten–Yee scheme, has the same form as the second-order Godunove-type TVD scheme when the piecewise constant characteristic speed is assumed to be $a_{j+1/2}$. (This Harten–Yee scheme was adopted throughout this study.) Thus $\phi^l_{j+1/2}$ of the lth characteristic field in equation (8) is expressed as

$$\phi^l_{j+1/2}=\sigma(a^l_{j+1/2})(g^l_j+g^l_{j+1})-Q(a^l_{j+1/2}+\beta^l_{j+1/2})\Delta_{j+1/2}\alpha^l. \tag{23}$$

Here $\Delta_{j+1/2}\alpha^l$ is the characteristic variable of the lth field, which is the lth component of the vector

$$\Delta_{j+1/2}\alpha=(\Delta_{j+1/2}\alpha^l)=R_{j+1/2}(U_{j+1,k}-U_{j,k}), \tag{24}$$

$a^l_{j+1/2}$ is the characteristic speed,

$$a^l_{j+1/2}=\tilde{u}_{j+1/2}\pm\tilde{c}_{j+1/2},\qquad \tilde{u}_{j+1/2}=\xi_x u_{j+1/2}+\xi_y v_{j+1/2},\qquad \tilde{c}_{j+1/2}=(\xi_x^2+\xi_y^2)^{1/2}c_{j+1/2}, \tag{25}$$

where $c_{j+1/2}$ is the sound speed, and g^l_j is the limiter,

$$g_j=\begin{cases}(\Delta_{j+1/2}\alpha^l\Delta_{j-1/2}\alpha^l+|\Delta_{j+1/2}\alpha^l\Delta_{j-1/2}\alpha^l|)/(\Delta_{j+1/2}\alpha^l+\Delta_{j-1/2}\alpha^l)\\ \qquad\text{for a non-linear field where } a=u\pm c,\\ s\max[0, \min(2|\Delta_{j+1/2}\alpha^l|, s\Delta_{j-1/2}\alpha^l), \min(|\Delta_{j+1/2}\alpha^l|, 2s\Delta_{j-1/2}\alpha^l)]\\ \qquad\text{for a linear field where } a=u,\end{cases} \tag{26}$$

where

$$s=\mathrm{sgn}(\Delta_{j+1/2}\alpha^l).$$

The functions $\sigma(z)$ and $\beta^l_{j+1/2}$ are expressed as

$$\sigma(z)=[Q(z)-\lambda z^2]/2, \tag{27}$$

$$\beta^l_{j+1/2}=\begin{cases}\sigma(a^l_{j+1/2})(g^l_{j+1}-g^l_j)/\Delta_{j+1/2}\alpha^l & \text{for } \Delta_{j+1/2}\alpha^l\neq 0,\\ 0 & \text{for } \Delta_{j+1/2}\alpha^l=0.\end{cases} \tag{28}$$

It should be noted here that the weak solution is not unique, hence there is a need for additional conditons to select the physically relevant solution. The additional requirement is that if $a_l>a>a_r$, the discontinuity remains as a shock wave (entropy conditon); if $a_l=a=a_r$, it remains as a contact discontinuity; and if $a_l<a<a_r$, the discontinuity must spread out as an expansion wave. Although the scheme shown by equation (21) in which $Q(z)=|z|$ does not guarantee the above-mentioned entropy condition, the numerical dissipation which is proportional to $|z|$ breaks up the discontinuity to an expansion wave if it is not a shock wave. However, if $|z|\to 0$ (i.e. in the vicinity of a sonic point), an unphysical discontinuity, namely an expansion shock, can exist owing to the zero dissipation. Therefore $Q(z)$ should be constructed in such a way that the zero dissipation is avoided, i.e.

$$Q(z)=\begin{cases}|z|, & |z|\geqslant\delta,\\ (z^2+\delta^2)/2\delta, & |z|<\delta,\end{cases}$$

$$\delta=\varepsilon(|u|+c),$$

$$\varepsilon=\begin{cases}\text{small positive number (e.g. 0.1)} & \text{for a non-linear field,}\\ 0 & \text{for a linear field.}\end{cases} \tag{29}$$

Note that an entropy correction for a linear field is not performed.

As the boundary condition on the wedge surfaces, the reflection condition was assumed by using the image point method. The grid used was not solution-adaptive. The computational grid system comprised 300×120 orthogonal and boundary-fitted grids. The computations were performed with the NEC SX-1 supercomputer of Tohoku University, Sendai, Japan.

In order to check the performance of the presently developed upwind TVD scheme, it was used to simulate the well-known 1D shock tube problem. Figure 4 illustrates the exact solutions (solid lines) and the numerical predictions (dots) for the density, pressure and velocity distributions. The initial conditions for this simulation were

$$u(x,0)=\begin{cases}U_L, & x\leqslant 0,\\ U_R, & x>0,\end{cases}$$

where

$$U_L=\begin{bmatrix}\rho_L\\ \rho_L u_L\\ e_L\end{bmatrix}=\begin{bmatrix}1\\ 0\\ 2{\cdot}5\end{bmatrix},\qquad U_R=\begin{bmatrix}\rho_R\\ \rho_R u_R\\ e_R\end{bmatrix}=\begin{bmatrix}0{\cdot}125\\ 0\\ 0{\cdot}25\end{bmatrix}.$$

A comparison between the exact solutions and the numerical predictions of the present simulation clearly indicates that the presently developed numerical code excellently reproduces the 1D shock tube problem.

$$U(x,0)=\begin{cases} U_L, & x\le 0 \\ U_R, & x>0 \end{cases}$$

$$U_L=\begin{bmatrix}\rho_L\\ \rho_L u_L\\ e_L\end{bmatrix}=\begin{bmatrix}1.0\\ 0.0\\ 2.5\end{bmatrix} \qquad U_R=\begin{bmatrix}\rho_R\\ \rho_R u_R\\ e_R\end{bmatrix}=\begin{bmatrix}0.125\\ 0.0\\ 0.25\end{bmatrix}$$

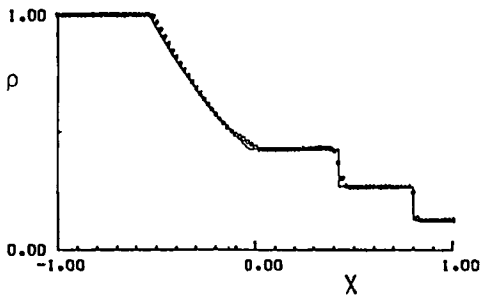

Density distribution

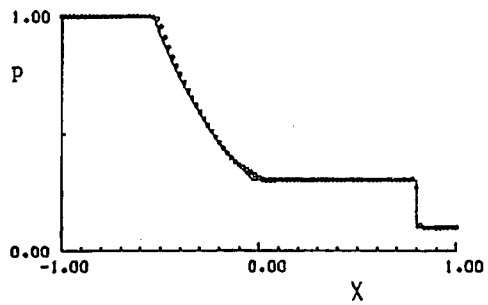

Pressure distribution

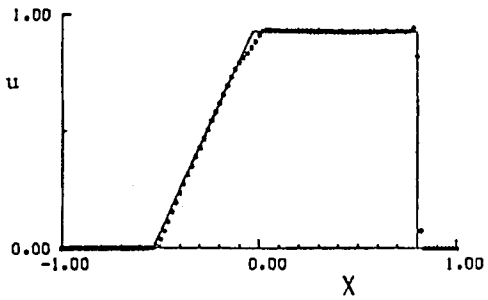

Velocity distribution

Figure 4. Comparison between exact solutions (solid lines) and numerical predictions (dots) of the classical 1D shock tube problem

EXPERIMENTS

The experiments were conducted using a 60 mm × 150 mm shock tube of the Shock Wave Research Center of the Institute of Fluid Science of Tohoku University. The driver section was 1.5 m long and had a diameter of 230 mm. The driver gas was air at room temperature. The length

of the driven section (the channel) was 8 m. The driven section ended at a damptank. The test section windows were made of BK7. Their dimensions were 150 mm × 230 mm. The test gas was dry air at room temperature. The initial pressure of the test section was varied in the range 30–80 kPa depending upon the desired value of the incident shock wave Mach number. The incident shock wave velocity was recorded using Kistler pressure transducers. These pressure transducers were flash-mounted in the upper wall of the shock tube just ahead of the test section. The attenuation of the incident shock wave was checked and found to be negligible.

Double-exposure holographic interferometry was used to record the reflection process. The light source was a Q-switched giant-pulse ruby laser ($\lambda = 694{\cdot}3$ nm) having a pulse width of 20 ns and an energy of about 1 J per pulse.

RESULTS AND DISCUSSION

Table II summarizes the initial conditions of the various experiments which will be discussed in the following. The experiments cover six of the seven domains of different reflection processes which are illustrated in Figure 3, and summarized in Table I.

The holographic interferograms of experiments 1–6 are shown in Figures 5(a)–10(a) respectively. Each holographic interferogram is accompanied by its corresponding numerical simulation (Figures 5(b)–10(b)) generated by the presently developed numerical code.

The actual isopycnics on Figures 5(a)–10(a) are labelled with letters starting with the letter 'a'. The density value which corresponds to each isopycnic appears in the table inset on each holographic interferogram. The density difference corresponding to one fringe shift is determined by the experimental set-up and is given as

$$\Delta\rho = \lambda/KL,$$

where λ is the wave length of the light source (694·3 nm), K is the Gladstone–Dale constant of the gas under investigation (approximately $0{\cdot}225\ \mathrm{cm^3\ g^{-1}}$ for air) and L is the width of the test section (60 mm). Therefore the density difference between two neighbouring fringes is $\Delta\rho = 5{\cdot}14 \times 10^{-5}\ \mathrm{g\ cm^{-3}}$. In order to compare the actual interferograms with the computational isopycnics, this value, normalized by the density ahead of the incident shock wave, was used to draw the computational isopycnics.

Figures 5(a) and 5(b) show the holographic interferogram and the computational isopycnics of a reflection process typical to domain 6 of Figure 3. A comparison shows that the triple-shock structure, the interaction of the reflected shock waves and the slip line which is initiated from the first triple point are well simulated by the numerical method. The secondary slip line which is generated when the two reflected shock waves intersect at the second triple point is not

Table II. Details of experiments

	Experiment no.	Domain in Figure 3	θ_w^1 (deg)	θ_w^2 (deg)	M_i	P_0 (kPa)
Concave double wedge	1	6	15	35	2·16	50·7
	2	7	20	55	2·16	30·4
	3	1	55	75	1·95	50·7
Convex double wedge	4	4	60	30	2·16	30·4
	5	3	35	15	1·49	66·7
	6	2	65	50	1·47	80·0

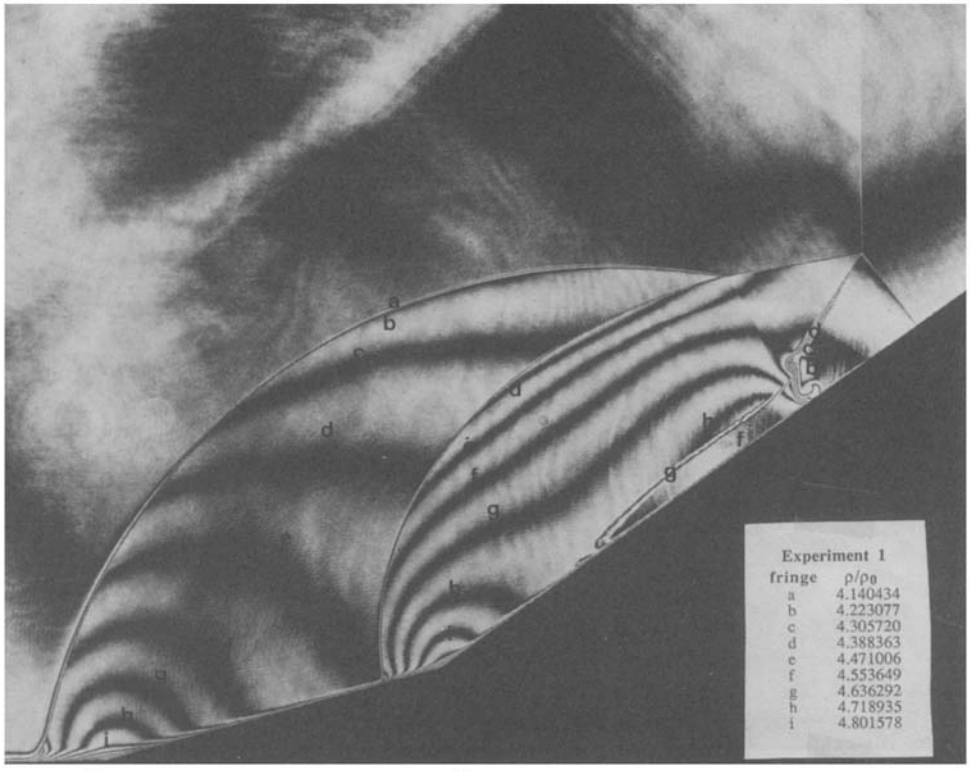

(a)

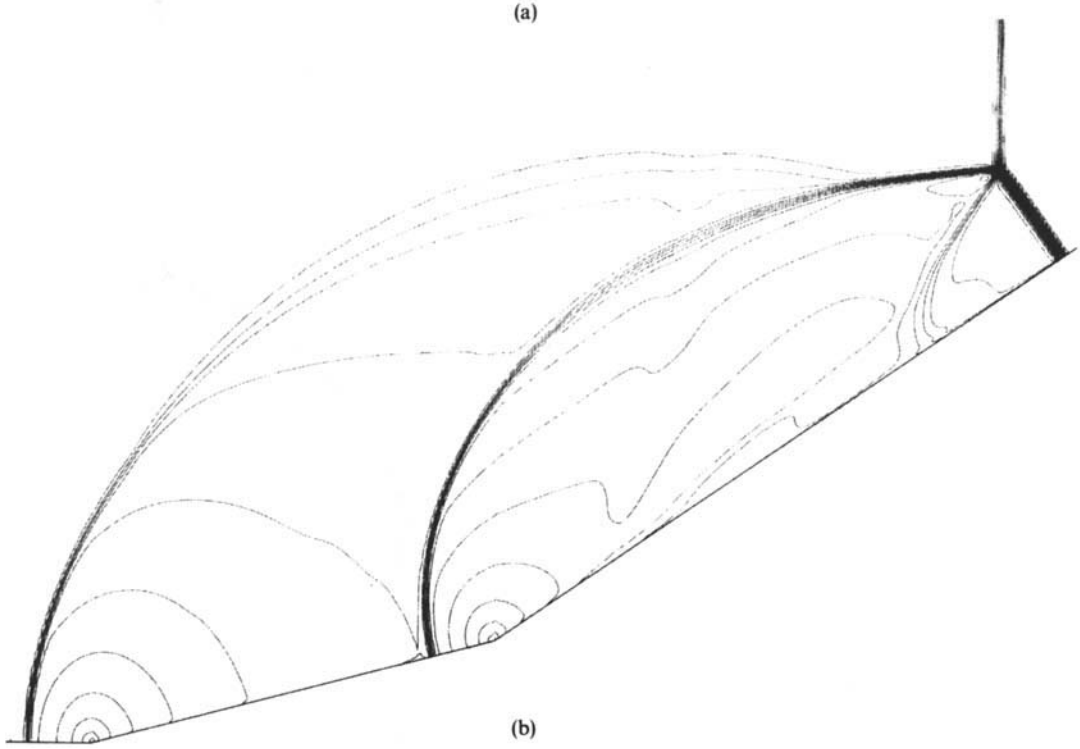

(b)

Figure 5. (a) Holographic interferogram of the reflection process in domain 6 of Figure 3; $\theta_w^1 = 15°$, $\theta_w^2 = 35°$, $M_1 = 2{\cdot}16$.
(b) Numerical simulation of interferogram shown in (a)

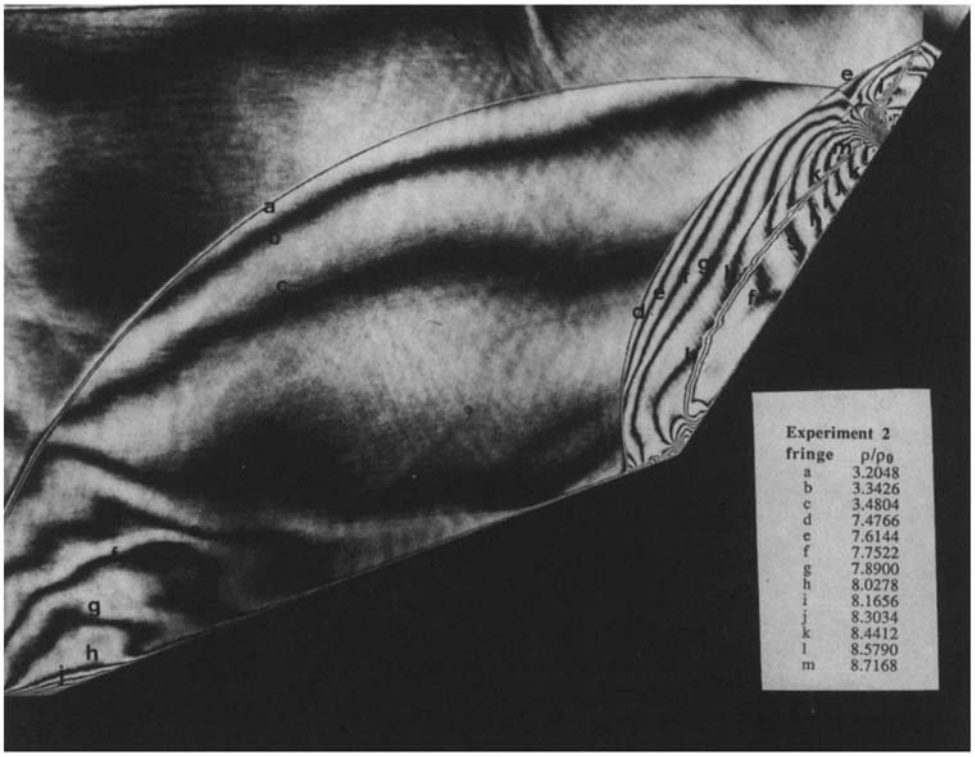

(a)

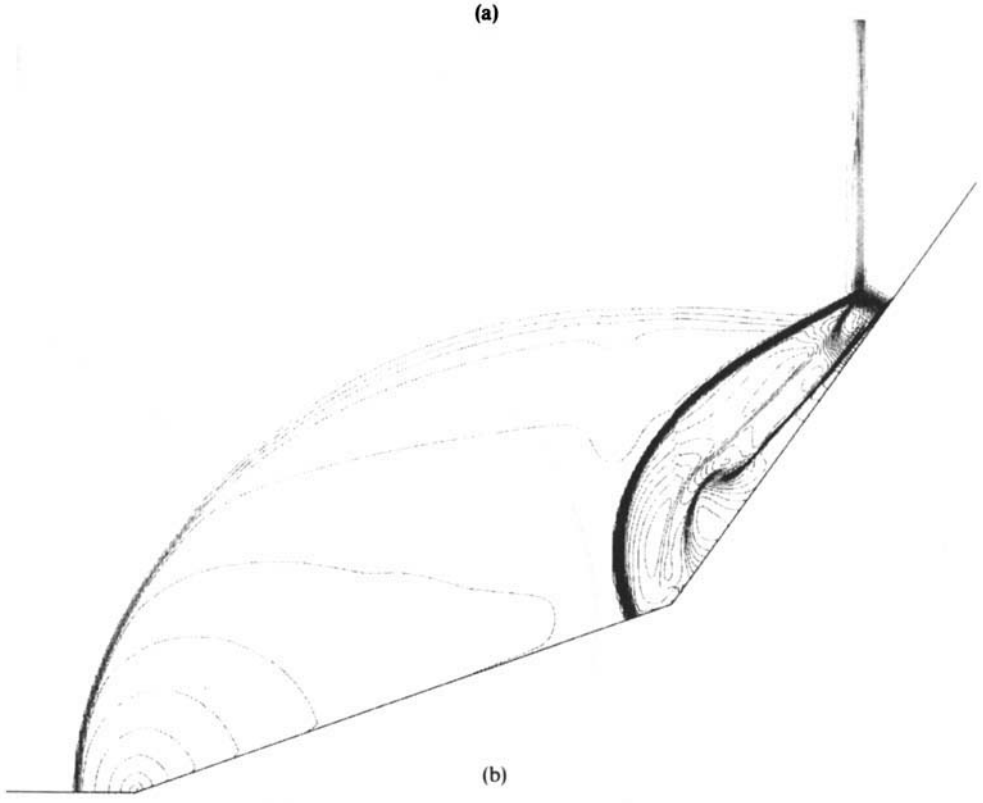

(b)

Figure 6. (a) Holographic interferogram of the reflection process in domain 7 of Figure 3; $\theta_w^1 = 20°$, $\theta_w^2 = 55°$, $M_i = 2{\cdot}16$.
(b) Numerical simulation of interferogram shown in (a)

reproduced by the simulation. However, its interaction with the first slip line is well reproduced. The interaction of the two slip lines results in a vortex which is also reproduced fairly well by the numerical simulation. This phenomenon, which is clearly observed in the interferogram, is not so clear in the numerical simulation, where the slip lines are diffusive and their interactions are not clearly resolved. Probably a finer mesh should be used and, moreover, the resolution should be improved in order to reproduce the detailed structure of the interaction of the slip lines. In addition, the general shape of the isopycnics is excellently reproduced by the numerical simulation.

The reflection process typical to domain 7 of Figure 3 is shown in Figures 6(a) and 6(b). In this case the triple point which appears in the first reflection propagates parallel to the second wedge surface. The wave interactions seem to be stronger than in the previous case. The first slip line seems to be parallel to the second surface. The agreement between the simulation and the experiment is fairly good except in the region where the slip lines interact. The secondary slip line is again not reproduced by the numerical simulation; however, its interaction with the first slip line is clearly reproduced.

Figures 7(a) and 7(b) show the reflection process typical to domain 1 of Figure 3. Although the strong wave interactions are observed only in the small region around the leading edge of the second reflecting wedge, they are well simulated by the present numerical solution. In addition, it

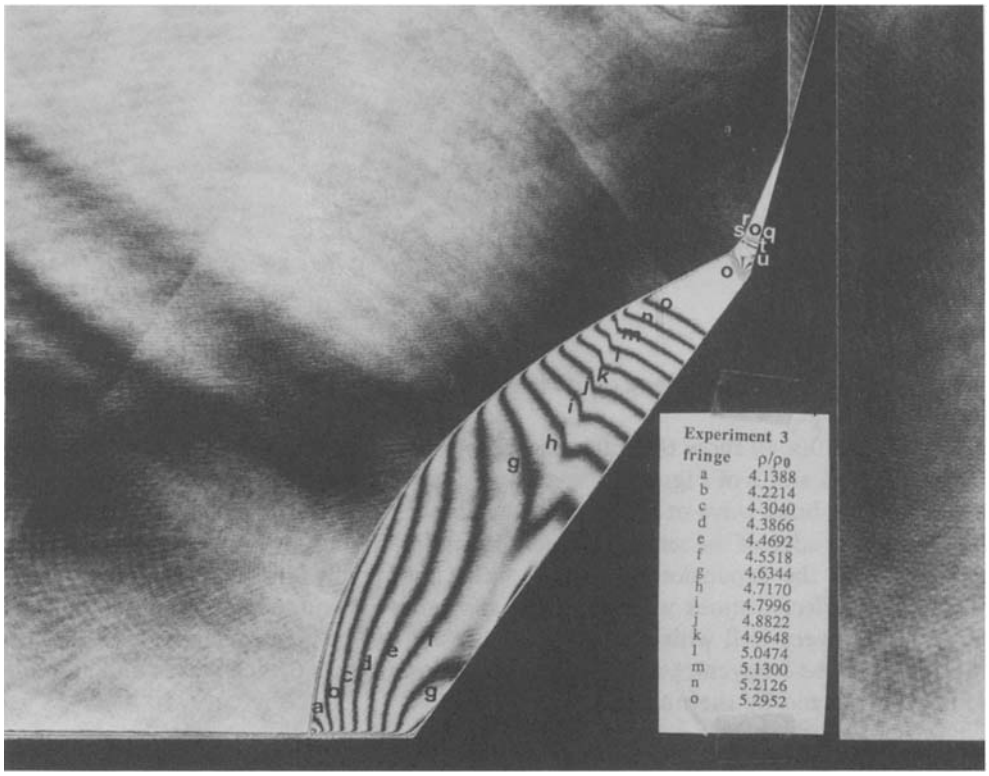

(a)

Figure 7. (a) Holographic interferogram of the reflection process in domain 1 of Figure 3; $\theta_w^1=55°$, $\theta_w^2=75°$, $M_i=1{\cdot}95$.
(b) Numerical simulation of interferogram shown in (a)

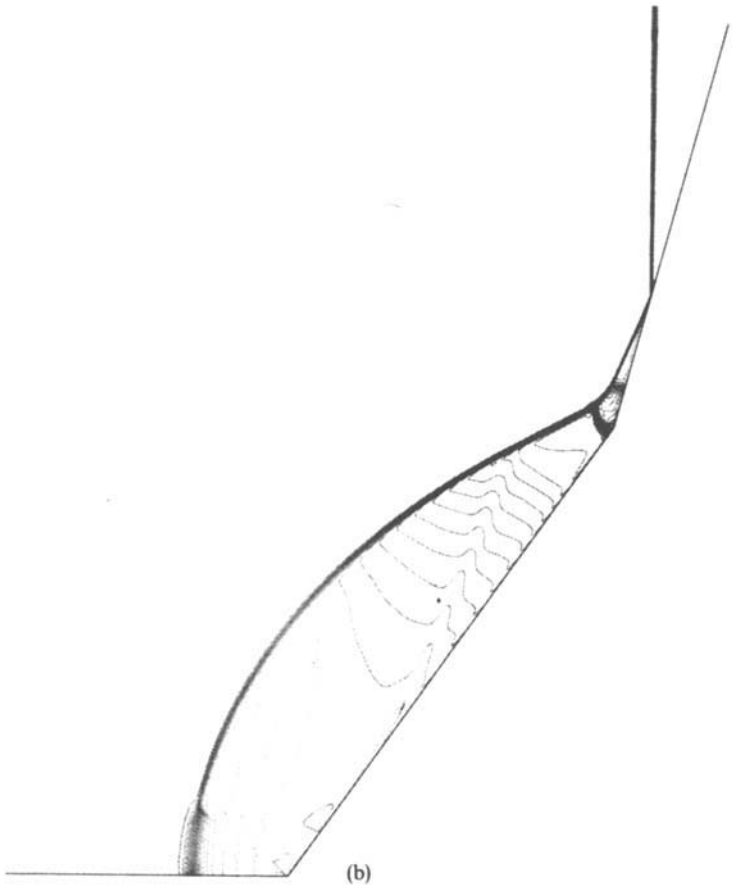

Figure 7. (Continued)

is clearly seen that the general shape of the isopycnics is excellently reproduced by the numerical simulation.

Figures 8(a, b)–10(a, b) show the reflection processes over convex double wedges corresponding to domains 4, 3 and 2 of Figure 3 respectively. In these cases expansion waves are generated when the incident shock wave or Mach stems, which are generated over the first surface, diffract around the leading edge of the second wedge surface. In addition, the interactions of the reflected shock waves with the expansion waves are well captured by the numerical simulation. The curvature of the reflected shock waves and the isopycnics around these interaction regions in the simulations agree very well with those obtained in the experiments. Finally, it is seen that the general shapes of the isopycnics and the various discontinuities (shock waves and slip lines) are excellently reproduced by the numerical simulations.

CONCLUSIONS

A numerical method based on the upwind TVD scheme was developed in order to simulate the various reflection processes of planar shock waves over concave and convex double wedges. The

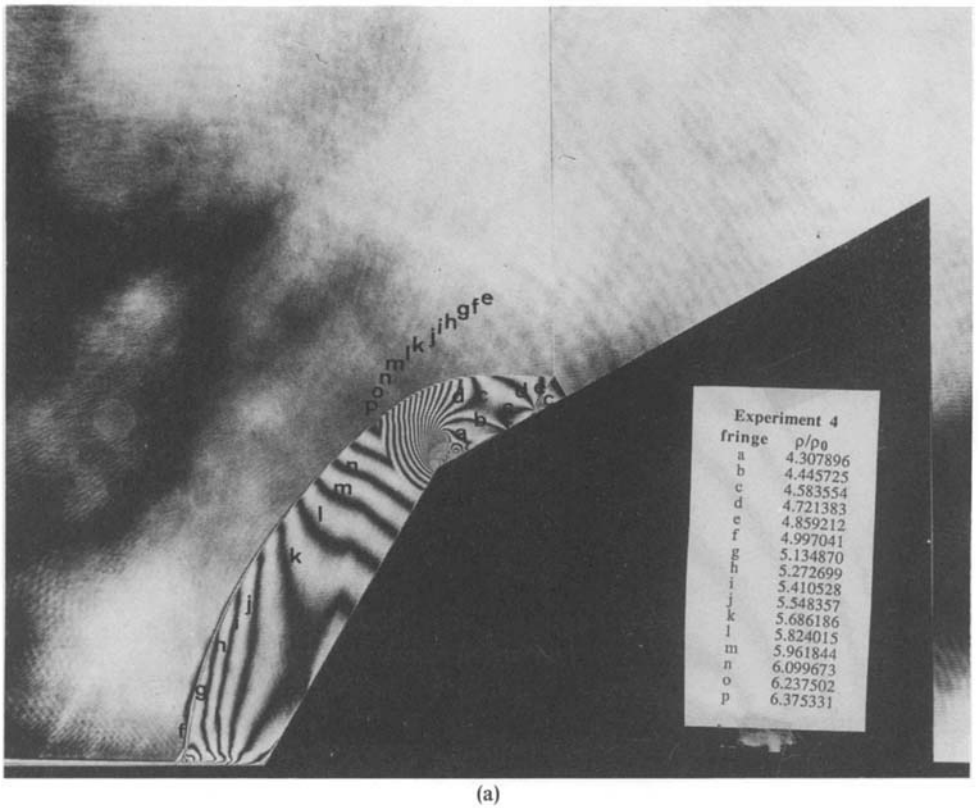

(a)

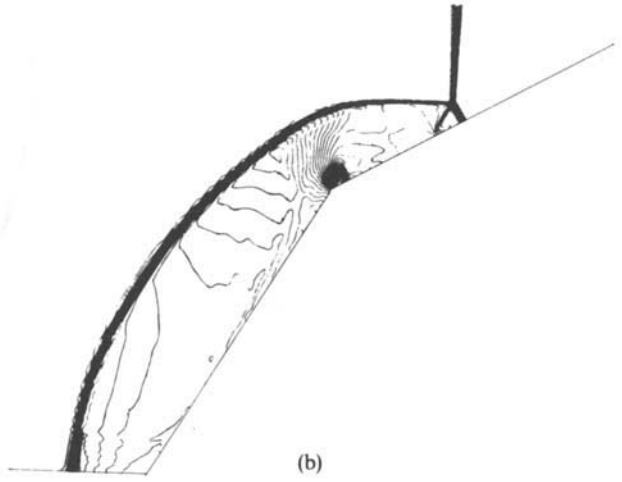

(b)

Figure 8. Holographic interferogram of the reflection process in domain 4 of Figure 3; $\theta_w^1 = 60°$, $\theta_w^2 = 30°$, $M_i = 2{\cdot}16$.
(b) Numerical simulation of interferogram shown in (a)

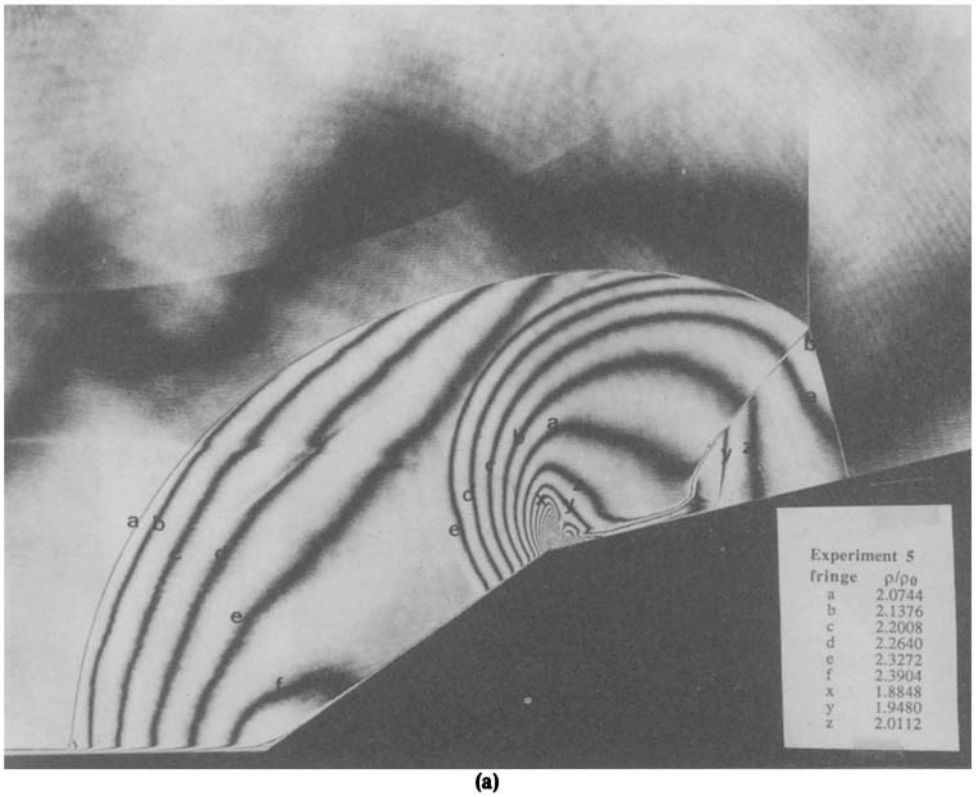

Figure 9. (a) Holographic interferogram of the reflection process in domain 3 of Figure 3; $\theta_w^1 = 35°$, $\theta_w^2 = 15°$, $M_i = 1{\cdot}49$.
(b) Numerical simulation of interferogram shown in (a)

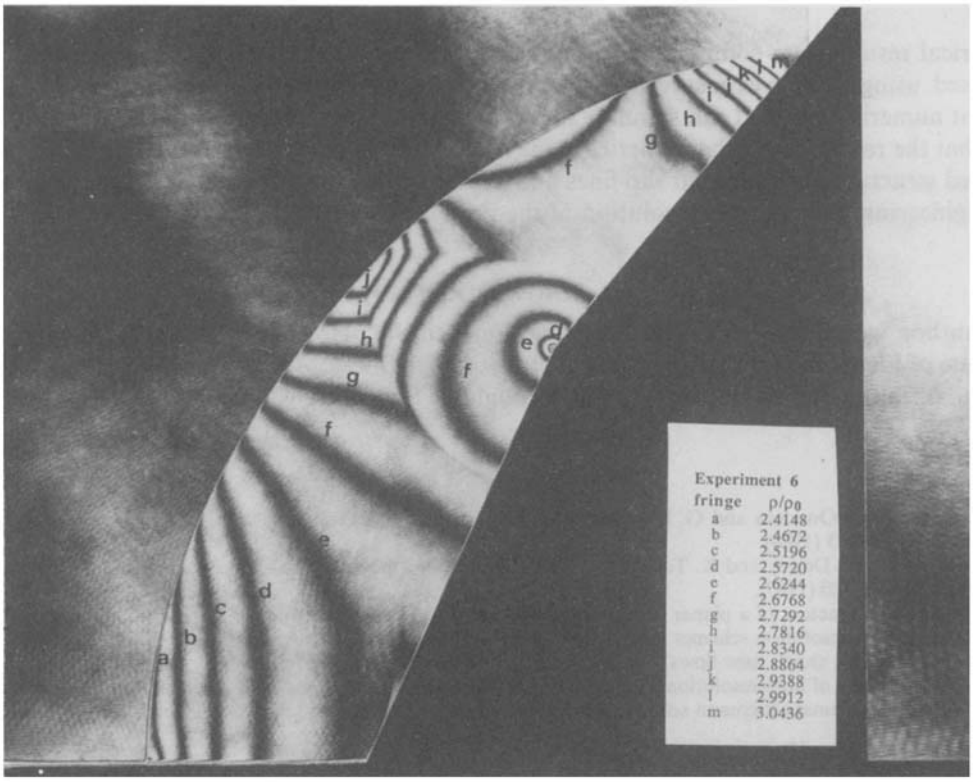

(a)

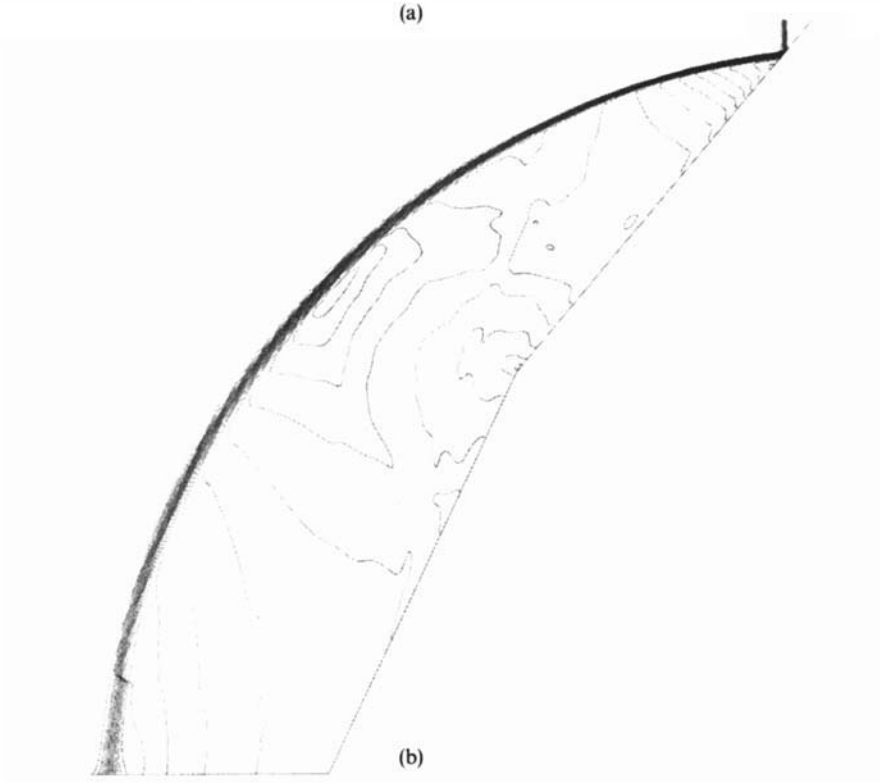

(b)

Figure 10. (a) Holographic interferogram of the reflection process in domain 2 of Figure 3; $\theta_w^1 = 65°$, $\theta_w^2 = 50°$, $M_i = 1{\cdot}47$.
(b) Numerical simulation of interferogram shown in (a)

numerical results were compared with results from actual shock tube experiments which were obtained using double-exposure holographic interferometry. The comparison shows that the present numerical method can simulate these complicated wave interactions fairly well. It shows also that the resolution of the numerical code needs to be improved in order to better resolve the detailed structure of the second slip lines and their interaction with the first slip lines. However, for engineering purposes the resolution of the present scheme could be considered satisfactory.

ACKNOWLEDGEMENT

The author would like to thank Professor Emeritus M. Honda, the former Director of the Institute of Fluid Science (formerly the Institute of High Speed Mechanics) of Tohoku University in Sendai, Japan, for his encouragement throughout the course of this research.

REFERENCES

1. K. Takayama, O. Onodera and G. Ben-Dor, 'Holographic interferometric study of shock transition over wedges', *SPIE*, **491**, 976–983 (1984).
2. G. Ben-Dor, J. M. Dewey and K. Takayama, 'The reflection of a plane shock wave over a double wedge', *J. Fluid Mech.*, **176**, 483–520 (1987).
3. G. Ben-Dor, 'Interaction of a planar shock wave with a double wedge like structure', *AIAA J.*, in the press (1991).
4. A. Harten, 'High resolution schemes for hyperbolic conservation laws', *J. Comput. Phys.*, **49**, 357–393 (1983).
5. K. Itoh, 'Transonic shock tube flows', *Ph.D. Thesis*, Tohoku University, Sendai, 1988.
6. H. C. Yee, 'A class of high-resolution explicit and implicit shock-capturing methods', *NASA TN 101088*, 1989.
7. P. L. Roe, 'Approximate Riemann solvers, parameter vectors, and difference schemes', *J. Comput. Phys.*, **43**, 357–372 (1981).